Boosting the anchoring and catalytic capability of MoS_2 for high-loading lithium sulfur batteries†

Zheng-Long Xu,[a*] Nicolas Onofrio,[b*] Jian Wang[c]

[a]Department of Industrial and Systems Engineering, The Hong Kong Polytechnic University, Hung Hom, Hong Kong, Email: zhenglong.xu@polyu.edu.hk

[b]Department of Applied Physics, The Hong Kong Polytechnic University, Hung Hom, Hong Kong, Email: nicolas.onofrio@polyu.edu.hk

[c]Department of Chemistry, Seoul National University, 1 Gwanak-ro, Gwanak-gu, Seoul 151-742, Republic of Korea

† Electronic supplementary information (ESI) available.

Abstract

High sulfur loading and low electrolyte/sulfur ratio are considered prerequisites for practically high energy lithium sulfur batteries (LSBs), however, shuttling and sluggish converting flooded polysulfides make it challenging to achieve full utilization of active materials with extended cyclic life. Herein, we explore 1T MoS_2 nanodots as powerful electrocatalyst to overcome this issue. Electrochemical and synchrotron *in-situ* X-ray diffraction characterizations reveal that 1T MoS_2 nanodots with numerous active sites are privileged to trap and propel the redox reactions for polysulfides. First principle calculations indicate that the surface and Mo-terminated edges of 1T MoS_2 provide stronger anchor sites for Li_2S, lower Li-S decomposition barrier and faster Li ion migration than those for 2H phase, a testament to the unique catalytic property for edge-rich 1T MoS_2 nanodots in LSBs. In the presence of a small amount of 1T MoS_2 nanodots, porous carbon/Li_2S_6 cathodes exhibit remarkable electrochemical performance retaining a capacity of 9.3 mAh cm^{-2} over 300 cycles under a high sulfur loading of 12.9 mg cm^{-2} and a low electrolyte/sulfur ratio of 4.6 μL mg^{-1}, which rivals with the state-of-the-art LSBs. Our combined experimental and theoretical analyses rationalize the use of nanodot catalyst in high energy rechargeable batteries.

1. Introduction

Lithium sulfur batteries (LSBs) with high theoretical energy densities of 2600 Wh kg^{-1} have been considered promising to take privilege over lithium ion batteries (LIBs) in meeting the emerging and demanding applications such as electric vehicle and smart grids.[1–3] However, the practical implementation of LSBs is plagued by several fundamental challenges, including the dissolution and shuttling of lithium polysulfides (LPSs), the insulating nature of sulfur and lithium sulfides, and the instability of Li metal anodes.[4] In the past decade, progress in structural design and materials chemistry has induced discernible improvement in battery performance.[5] For instance, a high sulfur utilization of 1620 mAh g^{-1} with long cycle life of 1000 cycles was reported for sulfur/graphene composite electrodes.[6] However, statistical analysis of the reported cathodes indicates that the major cathodes were tested under low sulfur loadings (<2 mg cm^{-2}) and high electrolyte/sulfur (E/S) ratios (>10 µL mg^{-1}), which are unacceptable for practical applications.[7–11] Based on theoretical estimations,[7,9] LSBs should possess sulfur loadings of above 7 mg cm^{-2}, areal capacities of over 6 mAh cm^{-2} and E/S ratios of less than 5 µL mg^{-1}, to outperform current LIBs in practical energy densities.

Increasing areal sulfur loading and decreasing the amount of electrolyte in cathodes are natural methods to meet above requirements. However, thick sulfur electrodes suffer cracking and peeling off problems during slurry casting,[12] damaging the electrode integrity. Another obstacle for thick electrode is the poor immersion of electrolyte,[13] which restrains effective sulfur utilization. A promising alternative approach is to use polysulfide solution, designated as catholyte, as the starting material.[14–19] The liquid catholyte is ready to immerse and envelope the surface of conductive host, facilitating rapid charge transfer at electrode/electrolyte interface, giving raise to fast reaction kinetics. In addition, highly concentrated catholyte possesses intrinsically low E/S ratio. For example, the E/S ratio of 1.5M Li_2S_6 catholyte is only 3.5 µL mg^{-1}, which is difficult to be achieved in sulfur particle electrodes. However, flooded

amounts of LPSs in carbon/catholyte electrodes induce severe shuttling effect due to the poor interaction between nonpolar carbon host and polar LPSs, leading to short cycle life.[19] Thus, introducing polar electrocatalysts in carbon/catholyte becomes imperative.

An ideal electrocatalyst is expected to provide a smooth "immobilization-diffusion-conversion" of LPSs to accelerate reduction kinetics and, hence boosting the electrochemical performance.[20,21] Nanostructured transition metal dichalcogenides,[22] especially MoS_2, have been proven effective in improving the sulfur utilization and battery cycle life by offering strong affinity to polysulfides. Typically, SnO_2/MoS_2 nanoarray,[23] MoS_{2-x}/reduced graphene oxide[24] and MoS_2/MOF derived carbon[25] have been prepared to enhance the cyclic stability and power capability of LSBs. Nevertheless, deep understanding of the correlation between atomic structure and catalytic activity of MoS_2 is still unclear. Attempt to maximize the catalytic capacity of MoS_2 has not been visited. Consequently, high contents of the inactive catalyst[26–28] were used to immobilize polysulfides (*i.e.*, 25.2 wt% of MoS_2 in MoS_2/graphene electrode),[27] significantly offsetting the high energy density of LSBs.

In this contribution, we propose to use a small amount of metallic 1T MoS_2 nanodot (ND, 3wt% of the electrode) as robust catalyst for advanced LSBs. Electrochemical tests and synchrotron *in-situ* X-ray diffraction (XRD) characterizations demonstrate strong anchoring and catalytic capability of MoS_2 NDs. When MoS_2 NDs are integrated with porous carbon/catholyte, the new cathodes exhibit remarkable battery performance, including a high rate capacity of 8.5 mAh cm^{-2} at 1C and an impressive capacity retention of 9.3 mAh cm^{-2} after 300 cycles under a high sulfur loading of 12.9 mg cm^{-2}, an extremely low E/S ratio of 4.6 uL mg^{-1} and a remarkable sulfur content of 81 wt%. The high energy densities delivered under high sulfur loading and lean electrolyte conditions are among the best so far reported for LSBs. Based on DFT calculations, we find that the phase and edge sites are the key governing the catalytical capability for MoS_2. Li_2S anchors preferentially at Mo-terminated edges of MoS_2

and the electrochemical dissociation occurs toward the surface of the monolayer where Li ions can diffuse faster. Indeed, the metallic 1T MoS_2 shows stronger affinity to polysulfides and lower activation energy of Li_2S than 2H MoS_2 at most of the adsorption sites. These findings suggest that the catalytic activity in MoS_2 can be maximized by downsizing 2H MoS_2 flakes to 1T MoS_2 NDs.

2. Experimental

2.1 Materials preparation

For 1T MoS_2 nanostructure preparation, 1T MoS_2 ND was prepared from the grinded small MoS_2 crystals via the chemical Li-intercalation using *n*-butyllithium as the intercalant.[29] Typically, 1 g of commercial 2H MoS_2 power (supplied by Aldrich) was put into a 100 mL grinding jar with 15-mm ZrO_2 grinding balls. The grinding jar was filled with Ar and sealed with parafilm in glovebox before grinding at 300 rpm for 3 h. Then, 0.1 g of grinded powder of 2H MoS_2 was immersed into 4 mL *n*-butyllithium solution (1.6 M in hexane, supplied by Aldrich) and kept in glovebox for 48 h to allow Li to intercalate into MoS_2 crystals. The mixture was then filtered and washed with hexane to remove the excess of *n*-butyllithium. The intercalated powder was thereafter exfoliated in water at 1 mg mL^{-1} through sonication for 1 h and centrifugation to remove large residuals. Large 1T MoS_2 sheet was prepared in the same way by using the pristine MoS_2 flakes without grinding.

For MoS_2/ carbon fiber (CF) electrodes preparation, as-prepared MoS_2 solution was dropped on CF cloth discs (Φ = 3/8 inch) and dried under vacuum. This procedure was repeated until the loading of MoS_2 reached 1 mg cm^{-2} for both MoS_2 ND/CF and MoS_2 sheet/CF electrodes, respectively.

For MoS_2/porous carbon electrodes preparation, exfoliated MoS_2 nanomaterials were dropped on porous carbon film using the same method as that for MoS_2/CF. The loading of MoS_2 nanostructure was controlled at about 3 wt% of MoS_2/porous carbon. The areal density

of MoS_2/porous carbon electrodes is about 3 mg cm^{-2}.[30] The porous carbon fiber electrode was prepared by electrospinning as our previous work.[30] Typically, 0.5 g polyacrylonitrile and 1.0 g iron (III) acetylacetonate were dissolved in 20 mL N,N-dimethyμformamide solvent by magnetically stirring at 80 ℃ overnight. The mixture was electrospun into nanofibers using an electrospiner at 18 kV, then the neat polymer nanofiber was stabilized in air at 220 ℃ and carbonized in Ar flow at 650 ℃. The resultant carbon fibers containing Fe_3C were etched using fuming HNO_3 to create mesopores by removing Fe_3C nanoparticles, followed with KOH chemical activation at 750 ℃. The mechanical stability of electrospun carbon nanofiber is strong enough that freestanding films were retained as electrodes.

For the preparation of electrolyte and polysulfide catholyte, the blank electrolyte was prepared by dissolving 1M lithium bis(trifluorometha nesulfonyl)imide (LiTFSI) in 1,3-dioxolane: 1,2-dimethoxy (DOL: DME 1/1 v/v) with 1 wt% $LiNO_3$ additive. Li_2S_8 solution was prepared by mixing sulfur and Li_2S with a molar ratio of 7:1 in tetraglyme solvent and magnetically stirred in an Ar-filled glove box at 50 ℃ for 8 h. The 1.5 M Li_2S_6 polysulfide catholyte was prepared by mixing stoichiometric amounts of sulfur and Li_2S in DOL/DME (1/1 v/v) solvent with 1M LiTFSI salt and 0.2M $LiNO_3$ additive. The concentration of catholyte was tunable by changing the solvent content. Note that the highly concentrated catholyte was stirred at 80 ℃ for 1 h before adding to MoS_2/porous carbon electrodes to ensure the well dissolution of active materials.

2.2 Materials characterization

The morphology and structure of MoS_2 were examined by scanning electron microscopy (SEM, Carl Zeiss, SUPRA) and transmission electron microscopy (TEM, JEOL, JEM-2100F). Dimensions of MoS_2 were investigated by a Dimension 3100 atomic force microscope (AFM) under ambient conditions. Samples for AFM test were prepared by dropping diluted MoS_2 solutions on cleaned mica substrates and dried on a spinner. Raman spectra were obtained from

a Horiba Jobin Yvon HR800 Raman microscopy equipped with a 488 nm laser operating at 180 mW. X-ray photoelectron spectroscopy (XPS, AXIS-His) was used to detect the chemical structures of MoS_2 and MoS_2/polysulfides in Ar atmosphere.

For synchrotron *in-situ* XRD characterization, holed coin cell was assembled and Kapton film with epoxy was used to seal the holes. The coin cell contained a MoS_2 ND/porous carbon/catholyte working electrode, a Li metal counter electrode and a 1M LiTFSI DOL/DME electrolyte soaked Celgard separator. The *in-situ* XRD experiment was conducted on a 3D XRD beamline at Pohang light source (PLS)-II with a wavelength $\lambda = 0.8265$ Å and the XRD data were collected as a set of circles on a Mar-345 image plate detector.[31] Accumulating the scanning time of the image and the transferring time of data together, the period between two data recording was about 3.5 min. The XRD data were periodically recorded during galvanostatic cycling of the coin cell at 0.2 C. Note that the 2θ angles from the raw XRD data were recalculated to corresponding angles for the wavelength of the general X-ray tube sources Cu Kα radiation ($\lambda = 1.543$ Å), for the purpose of convenient comparison with literature.

2.3 Cell assembly and electrochemical evaluation

To study the catalytic performance of MoS_2, potentiostatic reduction of Li_2S_8 (10 mM based on sulfur in tetraglyme solution) was conducted on CF-based current collectors. 25 µL Li_2S_8 was dropped onto the CF, MoS_2 sheet/CF and MoS_2 ND/CF current collectors as cathodes. CR2032 coin cells were assembled using as-prepared cathodes, Li metal anodes, Celgard separators and 25 µL 0.5M LiTFSI tetraglyme electrolyte. The cells were discharged to 2.06 V at 0.112 mA, to reduce all the long chain polysulfides to Li_2S_4. Then, the cells were kept potentiostatically at 2.05 V to drive nucleation and growth of Li_2S until the current dropped below 10^{-5} A. The current-time curves were integrated based on Faraday's law to evaluate the capacities from precipitation of Li_2S on various current collectors. To study the morphology of

precipitated Li_2S, the operated cells were dissembled in glovebox and washed with flooded DME before taking for SEM observation.

To study the redox kinetics of MoS_2 modified electrodes, cyclic voltammetry (CV), linear sweep voltammetry (LSV) and electrochemical impedance spectroscopy (EIS) measurements were performed. The CF, MoS_2 sheet/CF and MoS_2 ND/CF symmetric cells were prepared by assembling identical electrodes with Li_2S_4 catholyte. CV was conducted at an electrochemical workstation at a scan rate of 1 mV s^{-1} between -1 and 1 V. LSV studies were conducted using CF/Li_2S_4, MoS_2 sheet/CF/Li_2S_4 or MoS_2 ND/CF/Li_2S_4 as working electrodes and Li metal as counter electrodes. The cells were scanned from initial stage to 1.7 V *vs*. Li^+/Li at a scan rate of 0.1 mV s^{-1}. The half cells prepared for LSV study were also measured by EIS, where an amplitude voltage of 5 mV was applied over the frequency range from 100 kHz to 10 mHz.

For *in-situ* EIS examination, MoS_2 ND/porous carbon/0.5M Li_2S_6 catholyte and porous carbon/0.5M Li_2S_6 catholyte electrodes were prepared and assembled with Li metal as coin cells in an Ar-filled glove box. The *in-situ* EIS measurements were conducted on a Bio-Logic VSP-300 analyzer. After every 20 min galvanostatic discharge/charge at 0.1 C, the cells were held for 15 min to reach equilibrium before performing EIS measurement at a perturbation amplitude of 5 mV in the frequency range from 100 kHz to 10 mHz. The Nyquist plots were simulated using Z-view software.

To study the electrochemical performance, 1.5M Li_2S_6 catholyte was dropped onto MoS_2 ND/porous carbon, MoS_2 sheet/porous carbon and porous carbon free-standing electrodes with diameters of 3/8 inch. For low sulfur loading study, the amount of catholyte is 10 µL for each electrode and another 20 µL blank electrolyte was added to both cathode and anode sides. Therefore, the sulfur loading and E/S ratio were controlled about 4 mg cm^{-2} and 17.6 µL mg^{-1}. For high sulfur loading study, the amount of catholyte on MoS_2 ND/porous

carbon electrode was 32 µL and 10 µL blank electrolyte was dropped on Li metal side to wet separator. The sulfur loading and E/S ratio for high loading electrodes were calculated to be 12.9 mg cm^{-2} and 4.6 µL mg^{-1}. The sulfur content is calculated to be 81.1 wt% by taken the areal densities of MoS_2 ND/porous carbon (3 mg cm^{-2}) and sulfur (12.9 mg cm^{-2}) into account. MoS_2 ND/porous carbon/sulfur cathodes were prepared by melt-diffusion method. Typically, the porous carbon was mixed with sulfur particles at a mass ratio of 25:75 before heating at 155 ℃ for 12 h to impregnate sulfur with porous carbon. Then, MoS_2 ND was composited with porous carbon/sulfur in CS_2 solution.[30] The coin cells were cycled at different current densities between 1.7 and 2.8 V on a multichannel potentio-galvanostat (Won A Tech).

2.4 DFT calculation

Spin-polarized density functional theory calculations have been performed with VASP[32,33] with the Perdew, Burke, and Ernzerhof[34] exchange-correlation potential. Van der Waals interaction was incorporated using Grimme's DFT-D2 correction.[35] Convergence was achieved when energies and forces reached values lower than 10^{-6} and 10^{-5} eV, respectively. A kinetic energy cut-off of 550 eV was used to expand the plane-waves basis set. Two types of structures were studied including monolayers (2D-perdiodic) and strips (1D-periodic) of MoS_2. Monolayers were created by replicating 6 × 2 times the in-plane rectangular unit cells of 2H and 1T MoS_2 while strips were obtained by subsequently opening the *b*-direction of the supercells, resulting in both Mo- and S-terminated edges per strip. A vacuum space of approximatively 15 Å was imposed in the non-periodic directions. Gamma point calculations were performed for the strips while we used a 1×2×1 k-grid to compute integrals in the reciprocal space for the monolayers. Nudged elastic band calculations were performed to explore Li diffusion and Li_2S dissociation using slightly looser convergence criteria of 10^{-5} eV and 5×10^{-2} eV $Å^{-1}$ for energies and forces, respectively together with a kinetic energy cut-off of 400 eV. Binding energies were calculated as: $E_b = E_{Li2S}+E_{MoS2}-E_{Li2S@MoS2}$ with E_{Li2S}, E_{MoS2} and $E_{Li2S@MoS2}$ the energy of Li_2S, MoS_2 and

Li_2S adsorbed on top (or at the edge) of MoS_2, respectively. Following this definition, larger binding energy implies more favourable adsorption.

3. Results and discussion

3.1 Design of 1T MoS_2 nanodot catalyst

Ultrasmall 1T MoS_2 NDs were synthesized by chemical Li-intercalation of grinded 2H MoS_2 (~1 μm in size, Fig. S1, ESI†).[29] Large MoS_2 sheets were also prepared for comparison by Li intercalation in commercial 2H MoS_2 crystals (~20 μm in size, Fig. S1, ESI†). Fig. 1a shows TEM image of the exfoliated MoS_2 sheets, which present sizes of about 800 nm. High resolution TEM (HRTEM) image reveals a lattice parameter of 0.28 nm for the (100) plane of 1T MoS_2,[36] consistent with the diffraction spots in the inset of Fig. 1b. Fig. 1d shows uniform distribution of MoS_2 NDs with sizes of about 10 nm, and the NDs present lattice fringes of 0.28 and 0.65 nm, assigned to the (100) and (002) planes of 1T phase (Fig. 1e and Fig. S2, ESI†).[29] Dimensions of the two kinds of MoS_2 nanostructures were further characterized by AFM (Figs. 1c and 1f). The thickness × size of MoS_2 sheet and ND were statistically evaluated to be approximate 3.5 nm × 810 nm and 2.8 nm × 10 nm, respectively (Fig. S3, ESI†). Based on the dimensions of MoS_2 flakes, we can roughly calculate the exposed edge density by S_{edge}/S_{whole}, where S_{edge} and S_{whole} correspond to the surface area of edge and whole, respectively. When we regard MoS_2 sheets and NDs as rectangular prisms with equal edge lengths, the S_{edge}/S_{whole} for MoS_2 sheet and NDs were determined as 0.8% and 35.9%, respectively, indicating the dramatically increased edge surface area for NDs. When we plotted the particle number, the increase of edge surface area as a function of the particle size for MoS_2 prism, it is observed that the exposed edge surface area and the number of particles increase exponentially with downsizing MoS_2 sheet (Fig. 1g). Specifically, one MoS_2 sheet with size of 800 nm can be divided into 6,400 MoS_2 NDs of 10 nm in size and the edge surface area increases by 80 times, which favors the uniform distribution of catalysts on conductive substrates in LSBs.

The chemical structure of exfoliated MoS_2 was examined by Raman and XPS. A strong Raman peak at 143 cm^{-1} is observed for the exfoliated MoS_2 sheet and NDs (Fig. 1h), corresponding to fingerprint Mo-Mo stretching vibrations in 1T phase.[37] Peaks located at 194, 223, 289 and 350 cm^{-1} also refer to the phonon modes of 1T MoS_2.[37] For bulk MoS_2, only two typical Raman shifts at 377 and 403 cm^{-1} are identified, corresponding to the E_{2g}^1 and A_{1g} modes of 2H phase, respectively.[37,38] The phase identification for MoS_2 NDs was further investigated by XPS (Fig. 1i). The high resolution Mo 3*d* spectra can be deconvoluted into two dominant peaks located at approximate 231.6 and 228.5 eV, corresponding to the $3d_{3/2}$ and $3d_{5/2}$ components of 1T phase, respectively.[36] The Mo 3*d* peaks in MoS_2 NDs are ~1 eV lower than the counterparts in bulk 2H MoS_2 (Fig. S4, ESI†).[38] Similarly, the S 2*p* peaks of MoS_2 NDs located at about 162.5 and 161.7 eV, referring to $2p_{1/2}$ and $2p_{3/2}$, are also ~1 eV lower than the corresponding peaks for bulk 2H MoS_2 (Fig. S4, ESI†),[37] indicating the successful phase transition from 2H to 1T during Li intercalation.[38] And the percentage of 1T phase in MoS_2 ND is determined to be 92 % from XPS spectra. The morphological and structural characterizations demonstrate that MoS_2 NDs with intense edge sites and high purity of metallic 1T phase have been successfully prepared.

3.2 Catalytic behaviors of MoS_2 nanodots in polysulfides

To investigate the catalytic property of MoS_2 NDs on polysulfide reduction, we performed potentiostatic deposition of Li_2S from polysulfides (10 mM Li_2S_8 tetraglyme solution) on different substrates, including CF, MoS_2 sheet/CF and MoS_2 ND/CF. The electrodes were first discharged to 2.06 V to reduce most long-chain polysulfides before applying an overpotential of 0.01V to drive the precipitation of Li_2S.[30,39] The potentiostatic discharge curves of the three electrodes are shown in Fig. 2a. Fits of the capacity contributions of polysulfides reduction and the formation of Li_2S are represented by light red and blue colors, respectively (see the details in Fig. S5, ESI†). The quantity of Li_2S precipitations on MoS_2 ND/CF interface was calculated

to be 172.8 mAh g^{-1}, which is much higher than the 71.6 mAh g^{-1} for CF and 146.5 mAh g^{-1} MoS_2 sheet/CF electrodes. To validate the amount and morphology of Li_2S precipitates, we disassembled the discharged cells and observed with SEM. It reveals that three-dimensional Li_2S particles aggressively covered the MoS_2 ND/CF surface, and the amount of Li_2S on MoS_2 sheet/CF was slightly fewer, which are in sharp contrast to the arbitrary precipitation of Li_2S on bare CF surface (Fig. 2b). Chiang *et al* described that the nucleation and growth of Li_2S on conductive substrates follow classic chemical deposition theory along the polysulfide-Li_2S-substrate tri-phase boundary.[40] When the polysulfide absorptivity is enhanced and the reduction barrier is lowered simultaneously by electrocatalysts, phase transformation from liquid polysulfides to solid Li_2S will be profoundly promoted.[39,40] Thus, the largest reduction capacity and the three-dimensional Li_2S precipitates strongly indicate the highest catalytic capability for edge-rich MoS_2 NDs in polysulfide reduction. To study the potential of MoS_2 NDs in promoting Li_2S dissolution, we carried out galvanostatic charging of the lithiated MoS_2 ND/CF electrodes.[41] The initial charging voltage profiles of the discharged electrodes are shown in Fig. 2c. The MoS_2 ND/CF electrode exhibited a lower potential barrier at 2.21 V than the 2.38 V for MoS_2 sheet/CF,[42] implying potentially reduced energy barrier for Li_2S oxidation on MoS_2 ND/CF.

The reduction reaction kinetics was probed by LSV, symmetric CV and EIS of CF, MoS_2 sheet/CF, MoS_2 ND/CF electrodes in the presence of Li_2S_4 catholyte.[30] The MoS_2 ND/CF electrodes exhibit the highest current peak in LSV curves (Fig. S6, ESI†) and the largest exchange current density of 31.6 μA cm^{-2} calculated from Tafel plots (Fig. 2d), confirming the rapid kinetics of LPSs redox reactions. Symmetric CV measurements also show the highest current peak for the MoS_2 ND/CF electrodes (Fig. 2e). These results suggest that MoS_2 NDs, with strong chemisorption capability to LPSs, can serve as LPS promoter to tiger a rapid conversion in Li-S reduction reactions. The facilitated reaction kinetics is also supported by

the smallest charge transfer resistance for MoS_2 ND/CF electrode in EIS test (Fig. S6, ESI†). Overall, it is reasonable to conclude that the kinetics of soluble polysulfide reduction to insoluble lithium sulfides can be efficiently enhanced by MoS_2 ND catalyst, arising from the high chemisorption to LPSs, fast change transfer and abundant catalytic sites.

To probe the surface chemistry of MoS_2 NDs before and after LPS adsorption, XPS measurement was carried out. Fig. S7 (ESI†) shows the deconvoluted Mo 3*d* and S 2*p* spectra of pristine and polysulfides mixed MoS_2 NDs. In comparison with the pristine MoS_2 NDs, the Mo 3*d* peaks of $3d_{3/2}$ and $3d_{5/2}$ for MoS_2 ND/polysulfide overall downshifted by ~0.15 eV, which is attributed to the intense interaction of exposed Mo atoms with the surrounding strong electronegative sulfur ligand.[26,42] In the S 2*p* spectra, peaks centered at 163.2, 162.6 and 161.3 eV, corresponding to S $2p_{1/2}$ and $2p_{3/2}$ components of original MoS_2 ND, are almost intact after mixing with polysulfides, possibly due to weak interaction between S atoms in MoS_2 ND and polysulfides. Interestingly, new features located at 159.8 eV and 165.2-169.4 eV appeared for MoS_2 ND/polysulfide, which were denoted to the formation of polythionate moiety.[25] It is reasonable to deduce that the "sulfiphilic" surface for MoS_2 NDs would significantly promote the retention of polysulfides in cathode region. More importantly, the edge rich MoS_2 NDs increase the Mo-S bridge between metallic catalyst and polysulfides, propelling electron transfer across the MoS_2 ND to polysulfides, and thus significantly catalyzing the chemical redox conversion of polysulfides.

3.3 Theoretical modeling the interactions between lithium sulfides and MoS_2

To rationalize above experimental findings, we performed DFT calculations to explored the interactions between lithium sulfides and various sites of 2H and 1T MoS_2, including terrace (*i.e.*, on the surface), Mo-edge and S-edge sites. The corresponding binding energies are summarized in Table S1 (ESI†). From DFT-D2 calculations, the binding energies for Li_2S on terrace sites of 2H and 1T MoS_2 were determined to be 1.46 and 3.77 eV, respectively,

indicating stronger absorptivity of lithium sulfides for 1T phase. In addition, the 1T MoS_2 also shows stronger bond to Li_2S at Mo-edge sites than 2H MoS_2 (6.12 eV *vs*. 4.98 eV, respectively). Although 2H and 1T structures have similarities, our calculations indicate the phase dependent absorptivity of lithium sulfides on both terrace and edge sites. Indeed, 1T surface and Mo-edges represent stronger adsorption sites for lithium sulfides than 2H phase.

The electrochemical dissociation barriers of Li_2S on various sites were also studied. The molecular structure and the potential energy surfaces corresponding to these dissociations on 1T and 2H MoS_2 are presented in Fig. 3 and Fig. S8 (ESI†), respectively. On terrace sites, we found the electrochemical dissociation barrier of Li_2S is approximately 1.00 eV when adsorbed on the 2H surface of MoS_2, consistent with literature.[41] While this value reduces to only 0.56 eV on 1T phase. We note that the averaged bond length between Li-S was computed to be 2.10 Å in vacuum while 2.24 and 2.35 Å when adsorbed on the surface of 2H and 1T MoS_2, respectively. The mild elongation of the Li-S bonds on the surface of MoS_2 is consistent with physisorption. By contrast, when Li_2S is adsorbed on Mo-edges, bond lengths increased to 2.55 and 2.65 Å for 2H and 1T phases, respectively. This large bond elongation corresponds to spontaneous decomposition of Li_2S. We evaluated that it requires 0.66 and 0.52 eV of energy to further dissociate the Li-S bond at the Mo-edges of 2H and 1T MoS_2, respectively. We also computed the electrochemical dissociation of Li_2S adsorbed on 1T Mo-edge toward the surface of the monolayer to be 0.33 eV. When Li_2S is adsorbed on S-edge, Li-S bonds were evaluated to be partially dissociated with lengths of 2.48 and 2.40 Å and we further computed dissociation barriers of 0.10 and 0.37 eV on 2H and 1T structures, respectively. Furthermore, the activation barriers of Li diffusion on the surface of 2H and 1T MoS_2 were also calculated. We found similar migration barriers of 0.28 and 0.35 eV on the terrace of 2H and 1T MoS_2, respectively while adsorption of Li was found to be stronger on all sites for 1T phase of MoS_2.

To summarize, DFT calculations demonstrate that 1T phase of MoS_2 provides highly active adsorption sites on terrace and Mo rich edges for lithium sulfides immobilization and that the electrochemical dissociation of Li_2S prefers to occur on the surface or at the Mo-edges toward the surface of the monolayer where the Li ion can diffuse faster. These results suggest that marked increase of anchoring and catalytic capability comes from two equally important factors: the increase of edge atomic ratio and the high proportion of metallic 1T phase. Therefore, 1T NDs with numerous edge sites and metallic nature are expected to be ideal catalytic materials for LPS cathodes, consistent with above electrochemical results.

3.3 *In-situ* characterization of electrochemical behaviors

To examine the catalytic and capturing property of 1T MoS_2 ND in a working Li-S cell, MoS_2 ND/porous carbon/Li_2S_6 cathodes were prepared and subjected to synchrotron *in-situ* XRD and *in-situ* EIS characterizations. Fig. 4 shows the contour plot of *in-situ* XRD patterns collected during the first two cycles. Before discharging, no crystalline peaks were observed, confirming the high purity of polysulfide catholyte and the low content of MoS_2 NDs. When the cell was discharged to the plateau at 2.1 V, peaks referring to the (111) and (200) planes of cubic Li_2S (PDF No. 023-0369, marked with black dash line) appeared[43] and reached their maximum intensity at the end of lithiation (bottom of Fig. 4). Upon charging, the intensity of Li_2S decreased gradually, followed with no discernible XRD peaks and then generation of monoclinic S_8 (PDF No. 071-0137, marked with white dash lines),[43] illustrating the solid (Li_2S)- liquid (polysulfides) -solid (S_8) reactions during charging process. During the 2nd discharge/charge, reversible transitions between sulfur and Li_2S were observed. When we compare the current *in-situ* XRD result with peer studies,[43–47] two findings can be extracted. First, MoS_2 NDs propel the formation of Li_2S crystals. Nelson *et al*[44] and Yang *et al*[48] argued that the sluggish kinetics for solid (Li_2S_2)-solid (Li_2S) conversion prevents Li_2S formation upon full discharge of sulfur/carbon electrodes, resulting in undetectable Li_2S crystals during *in-situ*

XRD studies. The incomplete reduction accounted for deficient sulfur utilization and low reversible capacities. Fortunately, the powerful MoS_2 ND catalysts enable the reversible formation of crystalline Li_2S in our *operando* XRD studies. Second, Ye *et al*[46] reported that poor catalytic capability of MoN occasioned residual S_8 XRD peaks for MoN/sulfur electrode after full discharging, which is also observed for conventional 2H MoS_2 flakes modified porous carbon/Li_2S_6 cathodes in this work (Fig. S9, ESI†). In contrast, no residual sulfur/Li_2S crystals were observed for MoS_2 ND/porous carbon/Li_2S_6 after full discharging/charging, respectively, again indicating the high catalytic property for 1T MoS_2 NDs.

In-situ EIS is a powerful technique to probe the electrochemical impedance of a LSBs at different discharge/charge stages.[30,49] The discharge-charge curve for the second cycle and the correspondingly time-lapse EIS profiles of the MoS_2 ND/porous carbon/catholyte electrode are shown in Figs. 5a-c and controlling porous carbon/catholyte is presented in Fig. S10 (ESI†). The fitting line of a typical Nyquist plot clearly shows the impedance spectrum, which consists of the system resistance (R_s), electrolyte/electrode interfacial resistance (R_{suf}) and charge transfer resistance (R_{ct}) (Fig. 5d). Plots of all the resistances against depth of discharge (DOD) or state of charge (SOC) are shown in Fig. 5e. It is observed that MoS_2 ND/porous carbon/catholyte electrodes maintained a low R_{suf} of approximate 14 ohm during the whole discharge/charge, attributing to the strong entrapment and rapid conversion of polysulfides.[30] In contrast, R_{suf} for the porous carbon/catholyte electrode increased dramatically from 167 ohm to 579 ohm when DOD reaches 80% (Fig. S10, ESI†), suggesting severe migration of polysulfides and passivation of the electrodes. The R_{ct} for MoS_2 ND/porous carbon/Li_2S_6 slightly increases during discharging, stemming from the formation of insulating lithium sulfides. More importantly, R_{ct} of MoS_2 ND/porous carbon/catholyte is very much reduced compared to that for porous carbon electrode, indicating the strong affinity of MoS_2 ND to

polysulfides. These findings profoundly evidence the low interfacial resistances and robust LPSs anchoring performance for MoS_2 ND/porous carbon electrodes.

3.4 Electrochemical performance evaluation

The comprehensive electrochemical and theoretical investigations suggest that the MoS_2 NDs with strong LPS absorptivity and high catalytic property would be an ideal choice to robust electrochemical performance for LSBs. Thus, we systematically performed electrochemical measurements of MoS_2 ND/porous carbon/Li_2S_6, in comparison with porous carbon/Li_2S_6 and MoS_2 sheet/porous carbon/Li_2S_6 cathodes. Fig. 6a shows the CV curves of MoS_2 ND/porous carbon/Li_2S_6 between 1.7-2.8 V *vs* Li^+/Li at a scan rate of 0.1 mV s^{-1}.[14–19] Two cathodic peaks at 2.26 and 2.01 V were delivered during the first scan, which are assigned to the reduction of long chain polysulfides to short chain Li_2S_4 and further to solid Li_2S.[15,16] The reversible oxidation of Li_2S to polysulfides and to sulfur are presented by two anodic peaks at 2.39 and 2.47 V, respectively.[15,16] In the following three cycles, overlap of the discharge/charge peaks evidently indicates the excellent reversibility of the MoS_2 ND/porous carbon/Li_2S_6 electrode. Note that a slight negative shift of the cathodic peak from 2.26 V at the 1st sweep to 2.28 V in following sweeps is observed, possibly due to the increased polarization as the starting material changing from liquid catholyte to solid sulfur from the 2nd cycle. The excellent reversibility was also confirmed by discharging/charging at 0.1 C for 100 cycles (Fig. 6b). The MoS_2 ND/porous carbon/Li_2S_6 electrode presented a capacity of 1107 mAh g^{-1} at 2nd cycle and retained 1020 mAh g^{-1} after 100 cycles, rendering a low capacity degradation rate of 0.08% per cycle. In contrast, the porous carbon/Li_2S_6 and MoS_2 sheet/porous carbon/Li_2S_6 presented much higher capacity fading rates of 0.5% and 0.19% per cycle, respectively (Fig. S11, ESI†).

The anchoring and catalytic effect of MoS_2 ND can be more clearly evaluated by cycling batteries at high current densities, which requires stronger regulation of LPS diffusion and higher redox reaction kinetics at the electrode/electrolyte interfaces.[50] MoS_2 ND/porous

carbon/Li_2S_6 electrodes exhibit discharge capacities of 1156, 1071, 993, 955, 919 and 883 mAh g^{-1} at 0.1, 0.2, 0.5, 1, 2 and 4 C, respectively (Fig. 6c). Accordingly, the capacity retention from 0.1 to 2 C was determined to be 79.5% for MoS_2 ND/porous carbon/Li_2S_6. Under the same measurement conditions, the capacity retentions for porous carbon/Li_2S_6 and MoS_2 sheet/porous carbon/Li_2S_6 are only 1.2% and 22.7%, respectively (Fig. S12, ESI†). Statistical analyses of the discharge/charge voltage profiles (Fig. S12, ESI†) reveal that MoS_2 ND/porous carbon/Li_2S_6 retains the largest amount of polysulfides and the highest conversion efficiency with increasing current densities among the three electrodes. It is worth noting that the highly conductive porous carbon film also contributes to the excellent performance of MoS_2 ND/porous carbon/Li_2S_6 by offering physical barrier and electron conductive pathway to polysulfides.

High sulfur loading and low E/S ratio are now considered necessary for LSBs to rival with commercial LIBs.[7–11] Manthiram *et al*. recently proposed a "five 5s" critical metrics (*i.e*., sulfur loading >5 mg cm^{-2}, E/S ratio <5 µL mg^{-1}) for meeting the practical high energy Li-S systems.[11] Accordingly, we prepared MoS_2 ND/porous carbon/Li_2S_6 with a high sulfur loading of 12.9 mg cm^{-2}, a low E/S ratio of 4.6 µL mg^{-1} and a high sulfur content of 81 wt% (based on the total mass of electrode), and the electrochemical performance is shown Figs. 6d and 6e. The high-loading cathode is capable to present a high capacity of 856 mAh g^{-1} and a distinct discharge plateau of 2.09 V at 0.05 C, suggesting effective utilization of active materials under starved electrolyte. Further increasing the current density by 20 times from 0.05 to 1 C, 76.6% of the initial capacity still retained, again indicating the considerable argument of reaction kinetics for MoS_2 ND/porous carbon/Li_2S_6 electrode. To further determine whether the new electrodes can retain the high sulfur utilization during long-term cycles, the cells were cycled at 0.05C for 300 cycles (Fig. 6e). The high-loading electrode exhibits remarkable areal capacities of 11.3 and 9.4 mAh cm^{-2} after the 1^{st} and 300^{th} cycles, which are more than two

times higher than the 4.0 mAh cm^{-2} for commercial $LiCoO_2$ cathodes.[30,39] To evaluate the performance standing of the high-loading MoS_2 ND/porous carbon/Li_2S_6 cathode among its peers,[14–18,30,39,50–53] we summarized the electrochemical performance of the recently reported catalyst-modified cathodes in terms of cycle life, cyclic areal capacity and E/S ratio in Fig. 6f and Table S2 (ESI†). It clearly illustrates that the E/S ratio of 4.6 µL mg^{-1} in this work is among the lowest and the cyclic areal capacity of 9.3 mAh cm^{-2} after 300 cycles of the current cathode outperforms all the peers at a high sulfur loading over 10 mg cm^{-2}, suggesting its promising application in practical high energy LSBs. It is worth noting that for wide comparison with cathodes using sulfur particle as active materials, we also prepared high-loading MoS_2 ND/porous carbon/sulfur composite cathodes (Fig. S13, ESI†), which delivered a high areal capacity of 6.2 mAh cm^{-2} after 100 cycles, rivaling with the state-of-the-art catalyst-modified sulfur cathodes (Table S2, ESI†).

To obtain strong immobilization and fast conversion kinetics for polysulfides, the concept of constructing highly adsorptive and catalyzing heterostructures has been widely developed, such as TiN-TiO_2,[39] MoN-VN,[46] and WS_2-WO_3.[53] In fact, the anchoring of polysulfides as well as Li_2S precipitation is a continuous multielectron redox reaction in a working battery, thus an integrated platform, such as 1T MoS_2 ND in this work, enabling smooth "immobilization-diffusion-conversion" is more appealing. The unique advantages for 1T MoS_2 ND can be summarized as following. (i) The edge-rich NDs with intrinsically strong affinity to polysulfides serve as anchoring sites for LPSs and accelerate their reduction, which contributes to the long cycle life and high sulfur utilization. (ii) The highly conductive and catalytic nature of 1T MoS_2 NDs uniformly loaded on conductive substrates can facilitate Li-S reaction kinetics (Fig. S14, ESI†) and reduce the cell resistance, which benefits the high rate performance of MoS_2 ND modified cathodes. (iii) The well-defined morphology and phase of MoS_2 maximize the active sites to fully demonstrate their potential for Li-S chemistry, which

enables the boosting of electrochemical performance with a small amount of electrochemical inert catalysts. In addition, post-mortem analyses revealed that MoS_2 NDs/porous carbon remained stable after cycling (Fig. S15, ESI†). To further determine whether the excellent catalytic performance of MoS_2 NDs can retain during long-term cycling, the MoS_2 ND/porous carbon/Li_2S_6 cathode was prolonged to 500 cycles at 0.5C (Fig. S16, ESI†), which exhibits a low capacity fading rate of 0.08% per cycle, directly indicating the stability of MoS_2 NDs as catalyst in long-term Li-S batteries. Finally, thanks to the facile fabrication method and the low content needed to improve LSB performance, large-scale application of 1T MoS_2 ND in high energy LSBs will not be problematic.

4. Conclusions

In summary, we attempted to approach the limit of the capability of MoS_2 ND as a catalyst to anchor polysulfides and boost reaction kinetics in high-loading LSBs. DFT calculations elucidated the correlation between atomic structure and the catalytic property of MoS_2. It reveals that MoS_2 shows edge preferential absorptivity and lower Li_2S dissociation energy on the Mo-edges and terrace sites of metallic 1T MoS_2 than semi-insulating 2H phase. These findings provide profound guidance toward design powerful 1T MoS_2 ND for LSBs. Comprehensive investigations, including electrochemical measurements, *in-situ* EIS and *in-situ* XRD confirmed that MoS_2 ND can effectively suppress the diffusion of polysulfides and significantly enhance the Li-S redox reaction kinetics in a working LSB. As a result, the new MoS_2 ND/porous carbon/catholyte electrode exhibited impressive electrochemical performance under a high sulfur loading of 12.9 mg cm^{-2} and a low E/S sulfur ratio of 4.6 µL mg^{-1}. This work is expected to stimulate more investigations on nanodot catalysts applied in high energy storage devices for example, alkaline metal-sulfur batteries.

Conflicts of interest

There are no conflicts to declare.

Acknowledgements

The work described in this paper was supported by a grant from the Research Committee of The Hong Kong Polytechnic University under project code 1-BE3M, and partially supported by the Research Grant Councile of Hong Kong with project No. 15303219. ZL Xu thanks Dr. S J Kim currently at Brookhaven National Laboratory in USA for TEM assistance, Dr P Li at KAIST for AFM test, and LL Zhai at PolyU for XRD assistance.

Notes and references

1 X. Ji, K. T. Lee and L. F. Nazar, *Nat. Mater.*, 2009, **8**, 500.

2 P. G. Bruce, S. a. Freunberger, L. J. Hardwick and J. M. Tarascon, *Nat. Mater.*, 2011, **11**, 172.

3 A. Manthiram, Y. Fu, S. Chung, C. Zu and Y. Su, *Chem. Rev.*, 2014, **114**, 11751.

4 R. Xu, J. Lu and K. Amine, *Adv. Energy Mater.*, 2015, **5**, 1500408.

5 Q. Pang, X. Liang, C. Y. Kwok and L. F. Nazar, *Nat. Energy*, 2016, **1**, 16132.

6 H. Chen, C. Wang, W. Dong, W. Lu, Z. Du and L. Chen, *Nano Lett.*, 2015, **15**, 798.

7 M. Hagen, D. Hanselmann, K. Ahlbrecht, R. Maça, D. Gerber and J. Tübke, *Adv. Energy Mater.*, 2015, **5**, 1401986.

8 H.J. Peng, J.Q. Huang, X.B. Cheng and Q. Zhang, *Adv. Energy Mater.*, 2017, **7**, 1700260.

9 R. Fang, S. Zhao, Z. Sun, D.W. Wang, H.M. Cheng and F. Li, *Adv. Mater.*, 2017, **29**, 1606823.

10 Z. L. Xu, J. K. Kim and K. Kang, *Nano Today*, 2018, **19**, 84.

11 A. Bhargav, J. He, A. Gupta and A. Manthiram, *Joule*, 2020, **4**, 285.

12 Y. Ye, F. Wu, Y. Liu, T. Zhao, J. Qian, Y. Xing, W. Li, J. Huang, L. Li, Q. Huang, X. Bai and R. Chen, *Adv. Mater.*, 2017, **29**, 1700598.

13 K. Sun, A. K. Matarasso, R. M. Epler, X. Tong, D. Su, A. C. Marschilok, K. J. Takeuchi,

E. S. Takeuchi and H. Gan, *J. Electrochem. Soc.*, 2018, **165**, A416.

14 H. Pan, J. Chen, R. Cao, V. Murugesan, N. N. Rajput, K. S. Han, K. Persson, L. Estevez, M. H. Engelhard, J. G. Zhang, K. T. Mueller, Y. Cui, Y. Shao and J. Liu, *Nat. Energy*, 2017, **2**, 813.

15 Z. Sun, J. Zhang, L. Yin, G. Hu, R. Fang, H.-M. Cheng and F. Li, *Nat. Commun.*, 2017, **8**, 14627.

16 L. Li, L. Chen, S. Mukherjee, J. Gao, H. Sun, Z. Liu, X. Ma, T. Gupta, C. V. Singh, W. Ren, H. M. Cheng and N. Koratkar, *Adv. Mater.*, 2017, **29**, 1602734.

17 S. H. Chung and A. Manthiram, *Adv. Mater.*, 2018, **30**, 1705951.

18 G. Li, W. Lei, D. Luo, Y. Deng, Z. Deng, D. Wang, A. Yu and Z. Chen, *Energy Environ. Sci.*, 2018, **11**, 2372.

19 L. Qie, C. Zu and A. Manthiram, *Adv. Energy Mater.*, 2016, **6**, 1502459.

20 D. Liu, C. Zhang, G. Zhou, W. Lv, G. Ling, L. Zhi and Q. H. Yang, *Adv. Sci.*, 2018, **5**, 1700270.

21 Y. Song, W. Cai, L. Kong, J. Cai, Q. Zhang and J. Sun, *Adv. Energy Mater.*, 2020, **10**, 1901075.

22 M. Jana, R. Xu, X.-B. Cheng, J. S. Yeon, J. M. Park, J. Q. Huang, Q. Zhang and H. S. Park, *Energy Environ. Sci.*, 2020, **13**, 1049.

23 M. Wang, L. Fan, D. Tian, X. Wu, Y. Qiu, C. Zhao, B. Guan, Y. Wang, N. Zhang and K. Sun, *ACS Energy Lett.*, 2018, **3**, 1627.

24 H. Lin, L. Yang, X. Jiang, G. Li, T. Zhang, Q. Yao, G. W. Zheng and J. Y. Lee, *Energy Environ. Sci.*, 2017, **10**, 1476.

25 Q. Wu, Z. Yao, X. Zhou, J. Xu, F. Cao and C. Li, *ACS Nano*, 2020, **14**, 3365.

26 Z. A. Ghazi, X. He, A. M. Khattak, N. A. Khan, B. Liang, A. Iqbal, J. Wang, H. Sin, L. Li and Z. Tang, *Adv. Mater.*, 2017, **29**, 1606817.

27 J. He, G. Hartmann, M. Lee, G. S. Hwang, Y. Chen and A. Manthiram, *Energy Environ. Sci.*, 2019, **12**, 344.

28 B. Yu, Y. Chen, Z. Wang, D. Chen, X. Wang, W. Zhang, J. He and W. He, *J. Power Sources*, 2020, **447**, 227364.

29 C. Tan, Z. Luo, A. Chaturvedi, Y. Cai, Y. Du, Y. Gong, Y. Huang, Z. Lai, X. Zhang, L. Zheng, X. Qi, M. H. Goh, J. Wang, S. Han, X. J. Wu, L. Gu, C. Kloc and H. Zhang, *Adv. Mater.*, 2018, **30**, 1705509.

30 Z.L. Xu, S. Lin, N. Onofrio, L. Zhou, F. Shi, W. Lu, K. Kang, Q. Zhang and S. P. Lau, *Nat. Commun.*, 2018, **9**, 4164.

31 J. Park, Z. Xu, G. Yoon, S. K. Park, J. Wang, H. Hyun, H. Park, J. Lim, Y. Ko, Y. S. Yun and K. Kang, *Adv. Mater.*, 2020, **32**, 1904411.

32 G. Kresse and J. Furthmüller, *Comput. Mater. Sci.*, 1996, **6**, 15.

33 G. Kresse and J. Furthmüller, *Phys. Rev. B*, 1996, **54**, 11169.

34 J. P. Perdew, K. Burke and M. Ernzerhof, *Phys. Rev. Lett.*, 1996, **77**, 3865.

35 S. Grimme, J. Antony, S. Ehrlich and H. Krieg, *J. Chem. Phys.*, 2010, **132**, 154104.

36 M. Acerce, D. Voiry and M. Chhowalla, *Nat. Nanotechnol.*, 2015, **10**, 313.

37 X. Geng, W. Sun, W. Wu, B. Chen, A. Al-Hilo, M. Benamara, H. Zhu, F. Watanabe, J. Cui and T. Chen, *Nat. Commun.*, 2016, **7**, 10672.

38 W. Chen, J. Gu, Q. Liu, R. Luo, L. Yao, B. Sun, W. Zhang, H. Su, B. Chen, P. Liu and D. Zhang, *ACS Nano*, 2018, **12**, 308.

39 Z.L. Xu, S. J. Kim, D. Chang, K.Y. Park, K. S. Dae, K. P. Dao, J. M. Yuk and K. Kang, *Energy Environ. Sci.*, 2019, **12**, 3144.

40 F. Y. Fan, W. C. Carter and Y.M. Chiang, *Adv. Mater.*, 2015, **27**, 5203.

41 G. Zhou, H. Tian, Y. Jin, X. Tao, B. Liu, R. Zhang, Z. W. Seh, D. Zhuo, Y. Liu, J. Sun, J. Zhao, C. Zu, D. S. Wu, Q. Zhang and Y. Cui, *Proc. Natl. Acad. Sci.*, 2017, **114**, 840.

42 H. Yuan, H.-J. Peng, B.-Q. Li, J. Xie, L. Kong, M. Zhao, X. Chen, J.Q. Huang and Q. Zhang, *Adv. Energy Mater.*, 2019, **9**, 1802768.

43 S. Waluś, C. Barchasz, J. F. Colin, J. F. Martin, E. Elkaïm, J. C. Leprêtre and F. Alloin, *Chem. Commun.*, 2013, **49**, 7899.

44 J. Nelson, S. Misra, Y. Yang, A. Jackson, Y. Liu, H. Wang, H. Dai, J. C. Andrews, Y. Cui and M. F. Toney, *J. Am. Chem. Soc.*, 2012, **134**, 6337.

45 J. Conder, R. Bouchet, S. Trabesinger, C. Marino, L. Gubler and C. Villevieille, *Nat. Energy*, 2017, **2**, 17069.

46 C. Ye, Y. Jiao, H. Jin, A. D. Slattery, K. Davey, H. Wang and S. Z. Qiao, *Angew. Chemie - Int. Ed.*, 2018, **57**, 16703.

47 K. R. Kim, K.-S. Lee, C.-Y. Ahn, S.-H. Yu and Y.-E. Sung, *Sci. Rep.*, 2016, **6**, 32433.

48 X. Yang, X. Gao, Q. Sun, S. P. Jand, Y. Yu, Y. Zhao, X. Li, K. Adair, L. Kuo, J. Rohrer, J. Liang, X. Lin, M. N. Banis, Y. Hu, H. Zhang, X. Li, R. Li, H. Zhang, P. Kaghazchi, T. Sham and X. Sun, *Adv. Mater.*, 2019, **31**, 1901220.

49 G. Tan, R. Xu, Z. Xing, Y. Yuan, J. Lu, J. Wen, C. Liu, L. Ma, C. Zhan, Q. Liu, T. Wu, Z. Jian, R. Shahbazian-Yassar, Y. Ren, D. J. Miller, L. A. Curtiss, X. Ji and K. Amine, *Nat. Energy*, 2017, **2**, 17090.

50 L. Kong, X. Chen, B. Q. Li, H.J. Peng, J.Q. Huang, J. Xie and Q. Zhang, *Adv. Mater.*, 2018, **30**, 1705219.

51 H. Lin, L. Yang, X. Jiang, G. Li, T. Zhang, Q. Yao, G. W. Zheng and J. Y. Lee, *Energy Environ. Sci.*, 2017, **10**, 1476.

52 Y. Li, C. Wang, W. Wang, A. Y. S. Eng, M. Wan, L. Fu, E. Mao, G. Li, J. Tang, Z. W. Seh and Y. Sun, *ACS Nano*, 2020, **14**, 1148.

53 B. Zhang, C. Luo, Y. Deng, Z. Huang, G. Zhou, W. Lv, Y. He, Y. Wan, F. Kang and Q. Yang, *Adv. Energy Mater.*, 2020, **10**, 2000091.

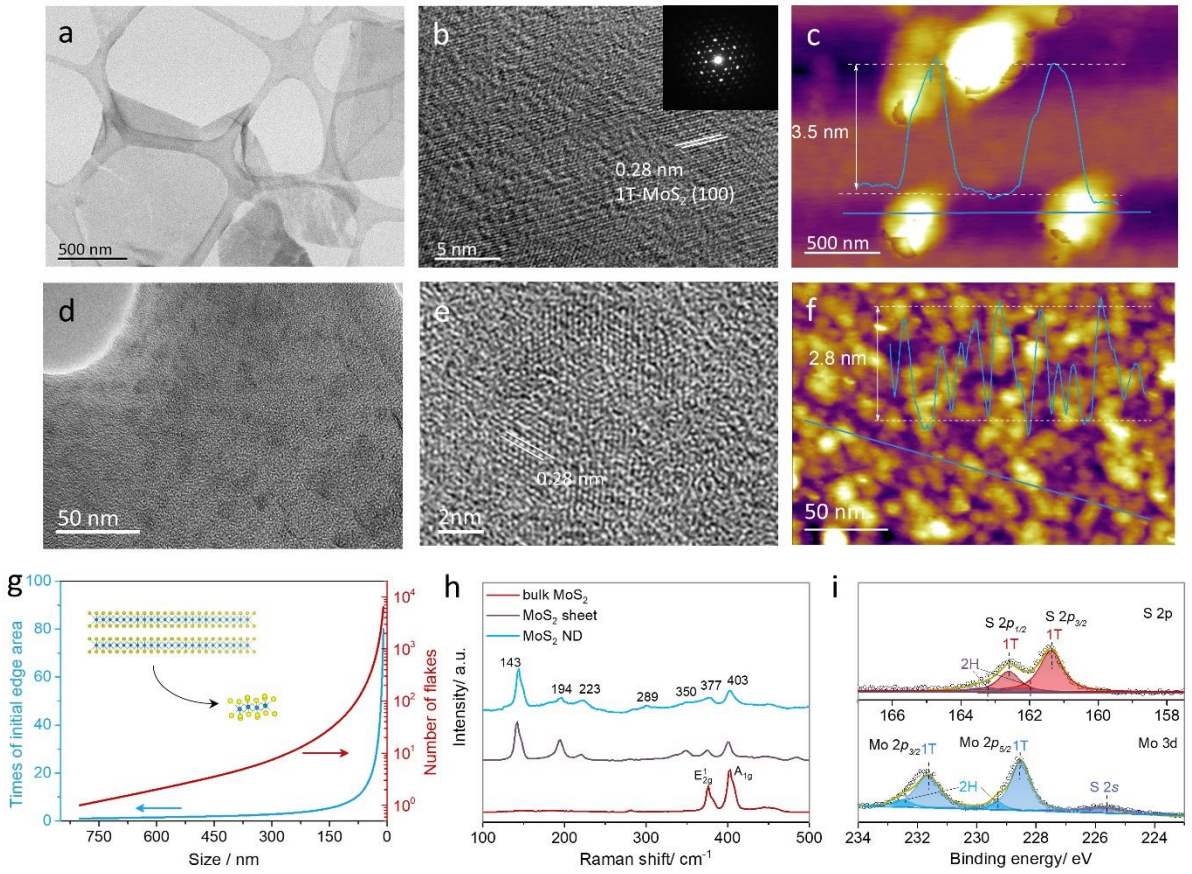

Fig. 1 Morphological and structural characterization of exfoliated MoS_2 nanostructures. (a) TEM, (b) HRTEM images of MoS_2 sheet. Inset in (b): The corresponding SAED pattern. (c) AFM height image of MoS_2 sheets. Inset in (c): The corresponding height profile along the blue dosh line. (d) TEM, (e) HRTEM and (f) AFM analyses of MoS_2 NDs. (g) The increase of exposed edge area and the number of flakes by downsizing a large MoS_2 sheet to MoS_2 NDs. (h) Raman spectra of bulk MoS_2 crystal (red), exfoliated MoS_2 sheet (purple) and MoS_2 NDs (blue) on a silicon substrate. (i) Deconvoluted XPS spectra of S 2*p* (up) and Mo 3*d* (down) for MoS_2 NDs.

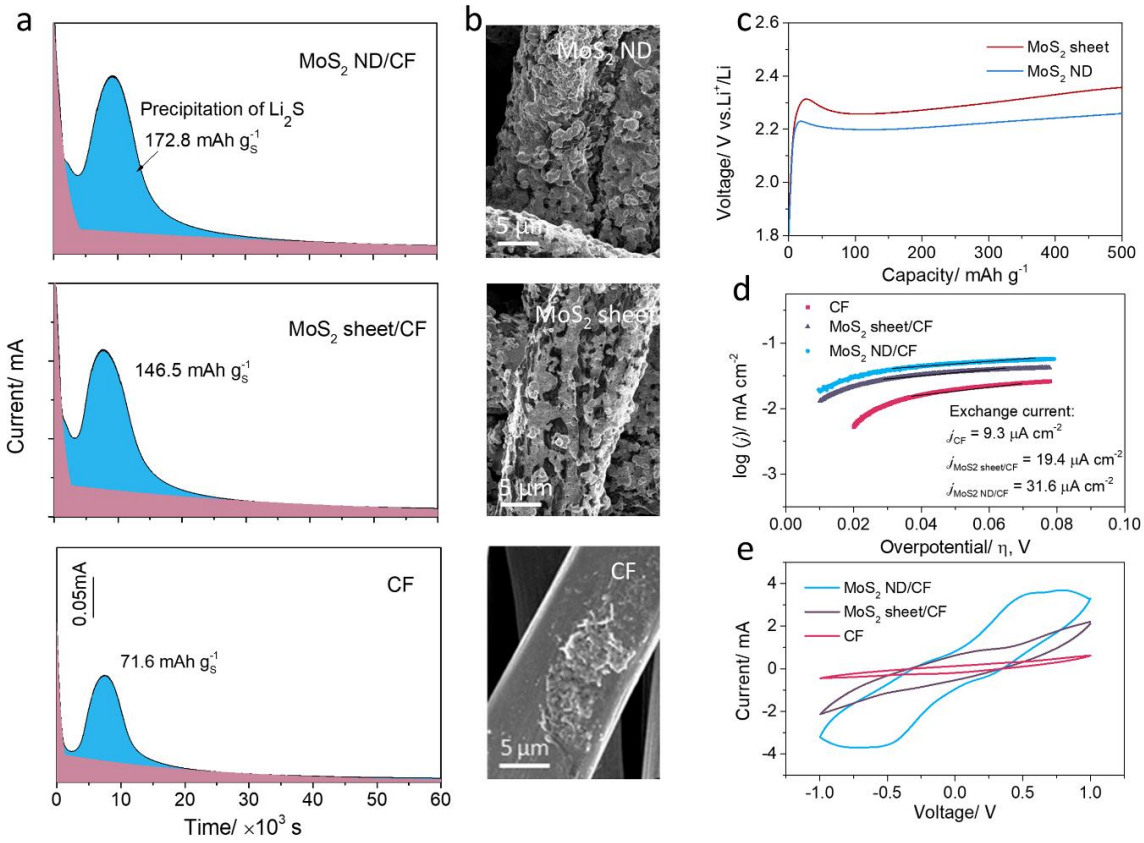

Fig. 2 Catalytic behaviors of MoS_2 NDs on polysulfides redox reactions. (a) Potentiostatic discharge curves of Li_2S_8 tetraglyme solution on CF, MoS_2 sheet/CF and MoS_2 ND/CF substrates. The light red and blue areas refer to the reduction of Li_2S_8/Li_2S_6 and the precipitation of Li_2S, respectively. (b) SEM images of the precipitated Li_2S on the three electrodes in (a). (c) The first charge voltage profiles of Li_2S on MoS_2 sheet/CF and MoS_2 ND/CF electrodes to show the electrochemical activation of Li_2S dissolution. (d) Tafel plots for CF, MoS_2 sheet/CF and MoS_2 ND/CF electrodes in catholyte, inset in (d): exchange current densities derived from (d). (e) CV of symmetric cells of CF, MoS_2 sheet/CF and MoS_2 ND/CF electrodes with Li_2S_8 catholyte.

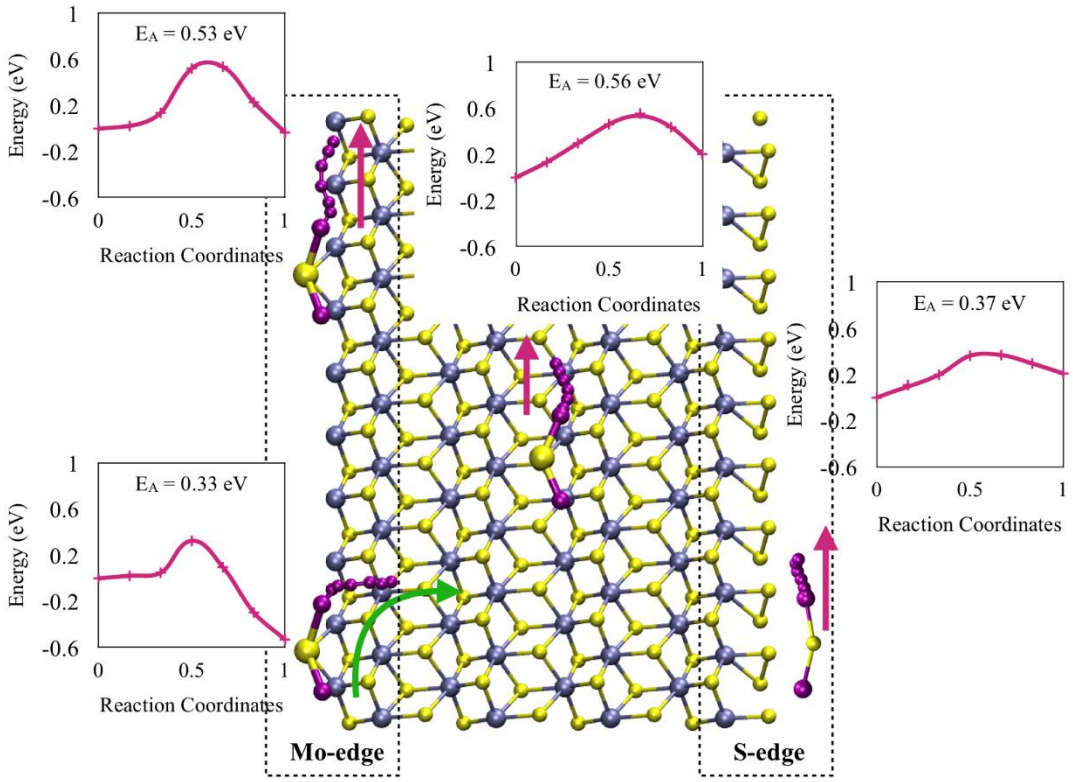

Fig. 3 First principle calculations of the electrochemical dissociation paths of Li_2S at various sites on 1T MoS_2. For each dissociation path, the potential energy surface and the corresponding activation energy are shown.

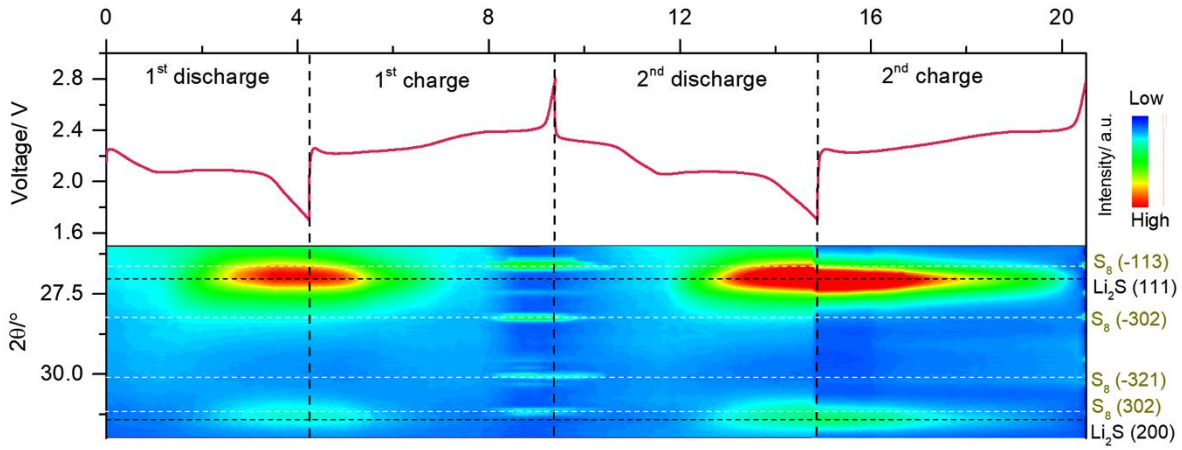

Fig. 4 *In situ* XRD measurements of MoS_2 ND/porous carbon/Li_2S_6 electrode during first two cycles. Top: galvanostatic voltage profiles. Bottom: XRD patterns of the electrode during cycling. The white and black horizontal dashed lines refer to S_8 and Li_2S, respectively. Red corresponds to high intensity and blue for low intensity.

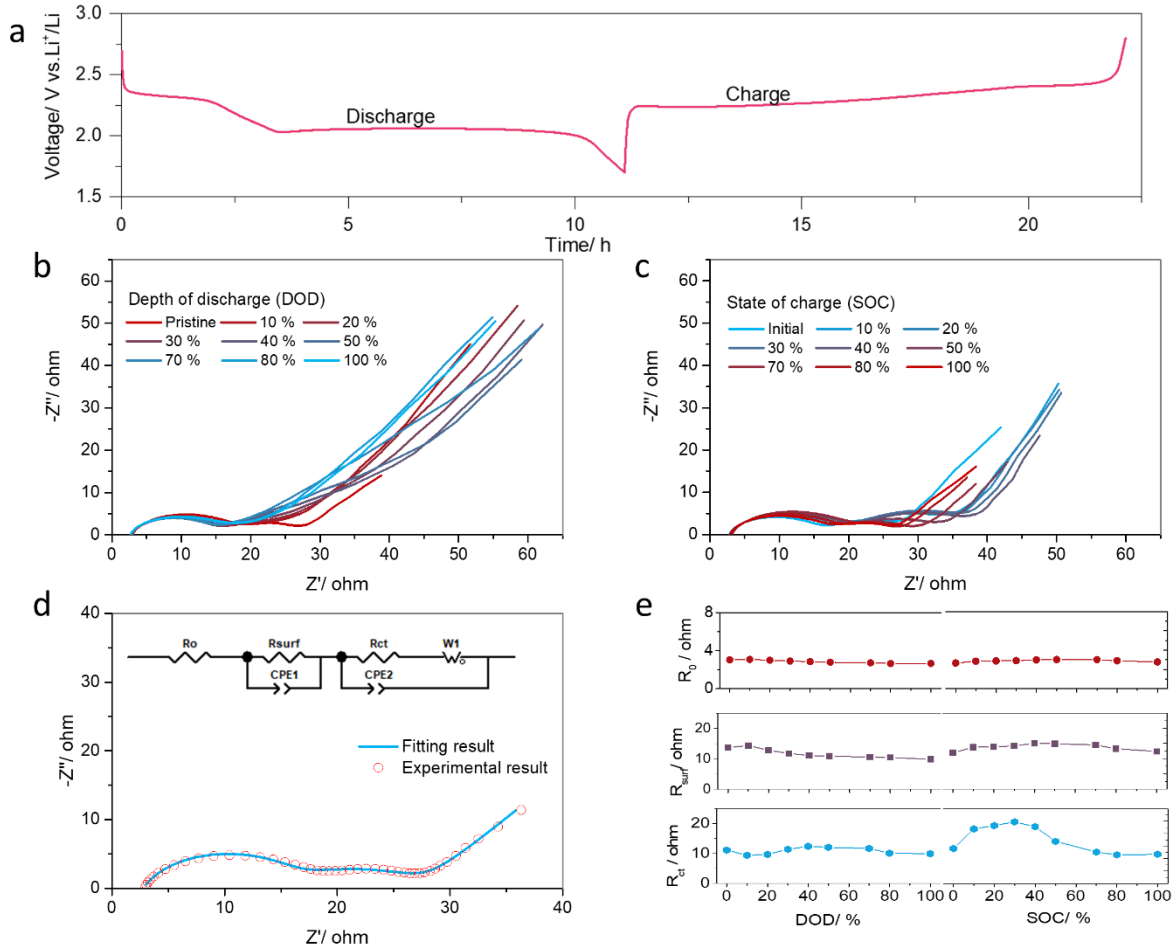

Fig. 5 *In-situ* EIS analysis of MoS_2 ND/porous carbon/Li_2S_6 cathodes. (a) Galvanostatic discharge/charge curve (the 2nd cycle) for the *in-situ* EIS study. (b) Nyquist plots at different depth of discharge (DOD). (c) Nyquist plots of the electrode at different state of charge (SOC). (d) A typical fitting result of the Nyquist plot measured at SOC of initial state, inset in (d) is the equivalent circuit model. (d) R_s, R_{suf} and R_{ct} derived from (b) and (c) plotted as functions of DOD or SOC.

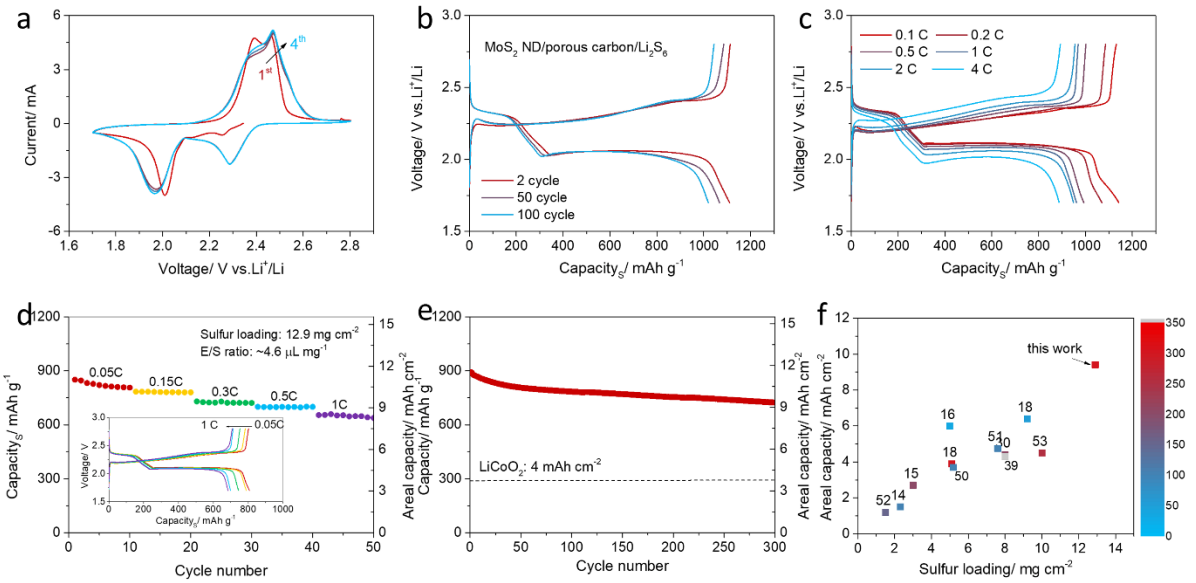

Fig. 6 Electrochemical performance for MoS_2 ND/porous carbon/Li_2S_6 electrodes. (a) CV for the first four cycles at a scan rate of 0.1 mV s^{-1}. (b) Voltage profiles at 0.1C for 2nd, 50th and 100th cycles. (c) Voltage profiles at current rates from 0.1 C to 4 C. (d) Rate capacities and (e) cyclic capacities for MoS_2 ND/porous carbon/Li_2S_6 electrodes under a high sulfur loading of 12.9 mg cm^{-2} and a low E/S ratio of 4.6 μL mg^{-1}. Inset in (d): discharge/charge profiles for the high loading LSBs. (f) Electrochemical performance comparison of MoS_2 ND/porous carbon/Li_2S_6 with peer electrodes in literature.[14–18,30,39,50–53]